

Quantum enhanced electric field mapping within semiconductor devices

D. Scheller^{1}, F. Hrunski^{1*}, J. H. Schwarberg², W. Knolle³, Ö. O. Soykal⁴, P. Udvarhelyi⁵, P. Narang^{6,7}, H. B. Weber⁸, M. Hollendonner^{1†}, R. Nagy¹*

¹*Institute of Applied Quantum Technologies, Friedrich-Alexander-University Erlangen-Nürnberg, 91052 Erlangen, Germany*

²*Chair of Electron Devices, Friedrich-Alexander-University Erlangen-Nürnberg, 91058 Erlangen, Germany*

³*Leibniz Institute of Surface Engineering (IOM), 04318 Leipzig, Germany*

⁴*Photonic Inc., Coquitlam, British Columbia, V3K 6T1, Canada*

⁵*Department of Chemistry and Biochemistry, University of California, Los Angeles, CA 90095, USA*

⁶*Division of Physical Sciences, College of Letters and Science, University of California, Los Angeles, CA 90095, USA*

⁷*Department of Electrical and Computer Engineering, University of California, Los Angeles, CA 90095, USA*

⁸*Chair of Applied Physics, Friedrich-Alexander-University Erlangen-Nürnberg, 91058 Erlangen, Germany*

** These authors contributed equally*

[†]*Author to whom any correspondence should be addressed, maximilian.hollendonner@fau.de*

Semiconductor components based on silicon carbide (SiC) are a key component for high-power electronics. Their behavior is determined by the interplay of charges and electric fields, which is typically described by modeling and simulations that are calibrated by nonlocal electric properties. So far, there are no experimental methods that allow for the 3D mapping of both the electric field and the concentrations of free charge carriers inside an electronic device. To fulfill this information gap, we propose an operando method that utilizes single silicon vacancy (V_{Si}) centers in 4H-SiC. The V_{Si} centers are at various positions in the intrinsic region of a *pin*-diode. To monitor the local static electric field, we perform Stark shift measurements based on photoluminescence excitation (PLE), which allows us to infer the expansion of the depletion zone and therefore to determine the local concentration of dopants. Besides this, we show that our measurements allow us to additionally obtain the local concentration of free charge carriers. The method presented here therefore paves the way for a new quantum-enhanced electronic device technology, capable of mapping the interplay of mobile charges and electric fields in a working semiconductor device with nanometer precision.

The performance of semiconductor devices is crucially determined by the complex interplay between charge carriers and electric fields. Models that balance microscopic quantities, like for instance the formation of depletion zones or the distribution of free charge carriers, have allowed to obtain an in-depth understanding of the underlying physical processes. Their validity was so far mainly confirmed

by comparing, for example, the resulting capacitance or current¹ as a function of the applied voltage, as electric fields and charge carrier distributions inside the semiconductor are not directly experimentally accessible^{2,3}. Nevertheless, these models paved the way for one of the greatest technological advances in history: semiconductor electronics.

The described interplay takes mainly place in the depletion zones between p and n doped regions. An externally applied voltage on a p or n doped region leads to local changes in the band structure [see Fig. 1 (a)], which is related to the spatial electric field E across the junction as

$$E = \frac{1}{e} \nabla \varepsilon_V(r). \quad (1)$$

Here $\varepsilon_V(r)$ is the energy of the valence band maximum and e the electron charge. It is therefore highly desirable to measure the electric field E with a high spatial resolution to gain a clear understanding of the device behavior.

It is only now that state-of-the-art quantum technology provides a way to microscopically investigate the interplay of electric fields and charges in a semiconductor component. A color center, placed inside a device, can be used as a highly sensitive and robust quantum sensor to map electric fields^{4,5} and charge densities. Such a quantum sensor offers the unique possibility to directly image a 3D electric field and provides a quantitative estimation of charge carriers inside a device and – even more sophisticated - during operation. These insights are currently only accessible by numerical simulations. Obtaining them experimentally may deliver more detailed information about the critical influence of imperfections in real devices and hence has the potential to shift what is technologically possible.

For our experiments we use 4H-SiC, which is a well-established material for high-power semiconductor electronic applications⁶. In addition, 4H-SiC is also an excellent host material for quantum technology applications⁷⁻⁹. Especially color centers inside the crystal lattice show excellent optical and spin properties¹⁰⁻¹⁴, establishing them as an ideal platform for quantum communication^{15,16}, quantum computing¹⁷⁻¹⁹, and quantum sensing²⁰⁻²³. Among the different color centers in 4H-SiC, the silicon vacancy (V_{Si}) center stands out due to significantly reduced spectral diffusion²⁴, the integrability into nanophotonic devices²⁵, and long spin coherence times^{26,27}. This makes the V_{Si} center a very promising candidate for quantum technology applications. A further advantage is the capability to integrate V_{Si} centers into semiconductor structures^{22,28}, which opens the unique possibility to monitor the interplay between electric fields and free charge carriers with nanometer resolution at various positions in an electronic device.

We show here the integration of V_{Si} centers into a pin -diode [see Fig. 1 (b)] for in-situ and even operando mapping of electric field measurements and determination of the charge carrier concentrations. For the measurements reported here spectroscopy of the V_{Si} center's narrow optical resonances between ground and excited state [see Fig. 1 (c,d)] is performed and we find frequency shifts of their positions due to the Stark effect. Besides this, we show that the voltage-dependent onset of the Stark shift in correlation with the spatial position of a V_{Si} center enables spatially resolved monitoring of the formation of an electric field across the pin -diode [see Fig. 1 (a)] and therefore, the local charge carrier information. Our results mark an essential step towards an improved understanding of a semiconductor device, as the method presented here can be used at arbitrary locations inside the material and allows to infer the physical parameters of the device with nanometer-resolution. Furthermore, we show that the voltage-dependent onset of the Stark shift is also present in optically detected magnetic resonance (ODMR) measurements. As ODMR is applicable at room

temperature, the method presented here paves the way for a new quantum-enhanced electric field mapping of semiconductor devices.

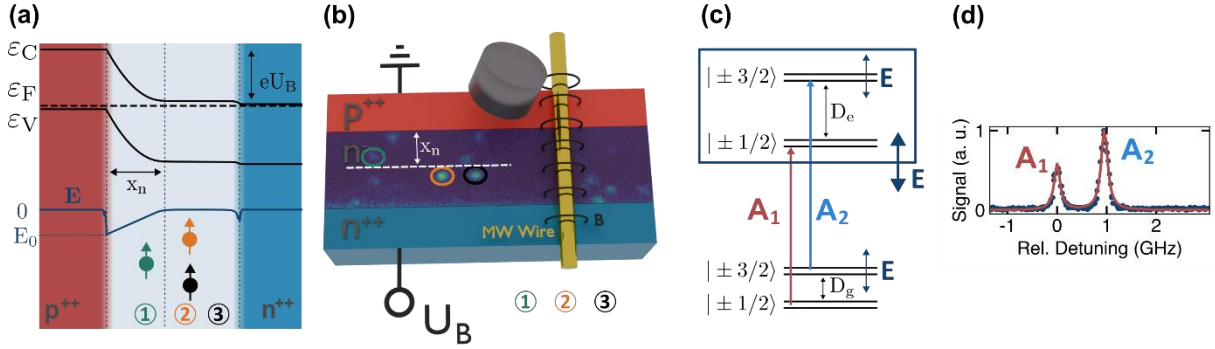


Figure 1: (a) The properties of a semiconductor device, including the electric field E , are determined by its band diagram and can be extracted via operando measurements at various points inside the low n -type doped layer (further referred to as “intrinsic layer” of the pin -diode). At the interface between p^{++} and the intrinsic layer, a depletion zone of width x_n forms, which can be determined via measurements of various V_{Si} centers. (b) Schematic of our setup, composed of a 4H-SiC pin -diode, a microwave (MW) wire for spin manipulation, and a high-NA objective for excitation and collection of the emission. Color centers at different positions inside the intrinsic region allow characterization of the semiconductor device, e.g., the extent of the depletion zone x_n . (c) Without a magnetic field, the $|\pm 1/2\rangle$ and $|\pm 3/2\rangle$ states are degenerate and connected to their excited states through A_1 and A_2 transitions. Axial electric fields influence both the ground (excited) state zero-field splitting D_g (D_e) as well as the zero-phonon-line between the ground and excited state with spin-dependent resonances A_1 and A_2 . (d) Both A_1 and A_2 transitions are identified via Photoluminescence-Excitation (PLE) measurements.

The used pin -diode’s n^{++} and p^{++} regions contain dopings in the range of $1 \times 10^{19} \text{ cm}^{-3}$ and are separated by a low n -type doped area of width $4.1 \mu\text{m}$, which we denote in the following as the intrinsic region of the diode. Based on our Stark shift measurements we find a concentration of dopants of around $9 \times 10^{14} \text{ cm}^{-3}$ (see discussion below), which deviates from the value specified by the manufacturer of $2 \times 10^{14} \text{ cm}^{-3}$. The V_{Si} centers within the sample are created via electron irradiation followed by an annealing step. Further information about the sample can be found in the Supplementary Information SI1. Our measurements are carried out at room temperature and 5 K. Optical measurements are performed with a homebuilt confocal microscope, where the optical resolution is diffraction limited at $> 500 \text{ nm}$. The sample is excited from a cleaved edge of the sample through a high-NA objective with a 730 nm laser for off-resonant and a tunable diode laser at 916 nm for resonant excitation. The emitted photons are filtered with a 950 nm long pass before being transmitted to a single photon detector with a quantum efficiency above 97 % for the emission spectrum of the V_{Si} center. The manipulation of the spin states is realized by an arbitrary waveform generator and a microwave wire on top of the sample. Detailed information about the home-built confocal setup is shown in the Supplementary Information SI2. For our measurements, we use the k - V_{Si} center (V_2). The V_{Si} center possesses a spin $S = \frac{3}{2}$ with two spin-conserving optical transitions, denoted as A_1 and A_2 [see Fig. 1(c)]. These two resonances can be detected by optical spectroscopy of the V_{Si} center’s fine structure, a method denoted as photoluminescence excitation (PLE) [Fig. 1 (d)]. The energy of both optical transitions depends mainly on axial electric fields, which can be taken into account via the Stark shift Hamiltonian^{29,30}:

$$H_{gs} = (D + d_z E_z) S_z^2. \quad (2)$$

Here $2D = 70 \text{ MHz}$ is the zero-field splitting (ZFS) of the k - V_{Si} , which is shifted by an axial electric field E_z . S_z is the axial spin-3/2 operator in the reference frame of the V_{Si} center, where the z -axis is defined by the c -axis of the 4H-SiC lattice. Contributions of transverse electric fields can be neglected, as the electric field is aligned with the c -axis of the crystal due to the device geometry, i.e. $E \parallel c$.

Eq. (2) indicates that the axial electric field induced by the *pin*-diode leads to a Stark shift of the optical transitions A_1 and A_2 which can be measured through PLE. An FEM-simulation of the electric field under the Lorentz local field approximation in dependence of the applied voltage is shown in Fig. 2 (a) (upper graph, further information about the FEM-simulations can be found in the Supplementary Information SI3). The electric field is generated by operating the *pin*-diode in reverse bias mode, where a positive voltage is applied on the n^{++} -doped area while the p^{++} -layer is grounded. The local electric field E at the position of the V_{Si} centers within the intrinsic layer increases with the applied reverse bias voltage up to $35.34 \frac{MV}{m}$ at 30 V. In the lower graph [Fig. 2(a)], three V_{Si} centers are color-coded at different positions in the intrinsic region ($1.61 \mu m$ and $2.71 \mu m$ from the p^{++} -layer). These V_{Si} centers are also shown with the same colors in the confocal map in Fig. 1 (b).

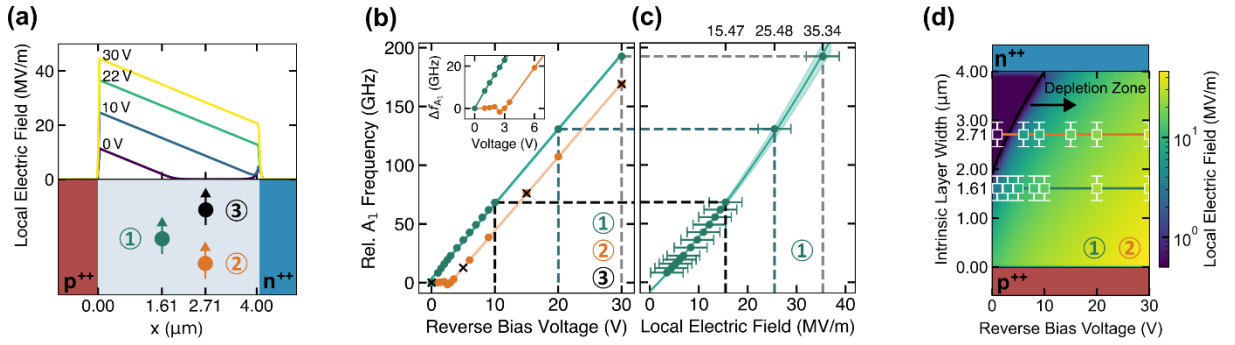


Figure 2: (a) Electric field, simulated across the intrinsic layer for voltages from 0 V to 30 V. (b) Measured shift of A_1 lines upon different applied voltages. Inset: The relative shift of the A_1 frequency (Δf_{A_1}) of V_{Si2} starts at around 2.6 V. (c) Stark shift of V_{Si1} as a function of the local electric field, incorporating electric field uncertainty due to uncertainty of the V_{Si} position (horizontal error bars). The shaded region displays the fit with 1-sigma uncertainty. Measurements of the PLE frequency in (b) allow for the reconstruction of the electric field values. (d) Simulation of the electric field distribution in the intrinsic layer, indicating that for 0 V V_{Si1} (green) is inside and V_{Si2} (orange) outside the depletion zone (black line). Dopant concentrations as used in the simulations entering into Fig. (c) and (d) is $9 \times 10^{14} cm^{-3}$. Vertical error bars in (b) and (c) are smaller than the data point.

We perform PLE measurements to determine the Stark shift caused by the electric field E within the intrinsic region. As can be seen from Fig. 2 (b), the A_1 transitions are shifted with respect to the applied voltage and we find that the relative distance between the optical transitions of A_1 and A_2 stays constant at $\approx 1 GHz$ (see Supplementary Information SI4). The Stark shift of V_{Si1} center (marked green in Fig. 2 (a)) increases linearly, but for $V_{Si2,3}$ centers (orange and black color code) the PLE frequency is only shifted for reverse bias voltages larger than $\approx 2.6 V$ [Inset Fig. 2 (b)]. This behavior can be understood by considering the depletion from the p^{++} into the intrinsic layer, which scales as $x_n(V) \propto \sqrt{(V + V_{bi})/N_D}$, in terms of the built-in voltage $V_{bi} = 2.95 V$ and N_D the concentration of dopants in the intrinsic layer. As V_{Si2} is located $2.71 \mu m$ away from the p^{++} -layer [Fig. 2 (a)], the voltage-dependent extension of the depletion region can be used to infer the concentration of dopants in the intrinsic layer, which we find to be $N_D = 9 \pm 2 \times 10^{14} cm^{-3}$ (see SI4 for the detailed calculation), resulting in a depletion region of $x_n = 1.9 \mu m$ for zero applied reverse bias voltage. This value is in good agreement with capacitance-voltage (CV) measurements (see SI1), yielding $N_D = 8.7 \times 10^{14} cm^{-3}$. By simulating the electric field [Fig. 2 (a,c)], the applied voltage can be converted into the resulting local electric field for $V_{Si1,2}$. The PLE shift is fitted with

$$\Delta f_{A_1} \propto -d \cdot E_z - \frac{\alpha}{2} E_z^2, \quad (3)$$

which allows to extract the dipole moment d and the polarizability α of V_{Si1} as, respectively, $|d| = 4.21 \pm 0.14 \frac{GHz}{\frac{MV}{m}}$ and $\alpha = -0.09 \pm 0.01 \frac{GHz}{\left(\frac{MV}{m}\right)^2}$ [Fig. 2 (c)]. These values are in good agreement with

the previously measured dipole moment of the k - V_{Si} of $d = 3.65 \frac{GHz}{\left(\frac{MV}{m}\right)}$ ³¹ and are comparable to first-principles estimates of the k - V_{Si} 's polarizability³² and experimental measurements of hexagonal silicon vacancy (h - V_{Si}) centers³³. A detailed discussion about the derived dipole moment and the polarizability can be found in SI6. Based on first-principles calculations, we determine $d = 1.83 \pm 0.01 \frac{GHz}{\left(\frac{MV}{m}\right)}$ and $\alpha = -0.0254 \pm 0.0006 \frac{GHz}{\left(\frac{MV}{m}\right)^2}$ (see SI7 for detailed information). The differences from our measured values are probably related to the functional used in the first-principles calculation and to piezo effects.

By measuring the PLE shift upon an applied reverse bias voltage, the electric field can be reconstructed, which in Fig. 2(b,c) is performed for voltages of 10 V, 20 V and 30 V, resulting in electric fields of, respectively, 15.47 MV/m, 25.48 MV/m and 35.34 MV/m. The presented measurement therefore opens the possibility to compare the measured electric fields against simulations of a semiconductor device [see data points in Fig. 2 (d)]. The sensitivity of the measurements presented in Fig. 2 is $14 \frac{kV/m}{\sqrt{Hz}}$ (see SI8), which is comparable to single NV-centers²⁹ in bulk diamond. As the electric break-down field of typical SiC devices is in the order of 328 MV/m³⁴, V_{Si} centers are therefore excellent quantum systems to infer the mechanisms of the device failure, e.g. the electric-field dependent onset of impact ionization³⁵.

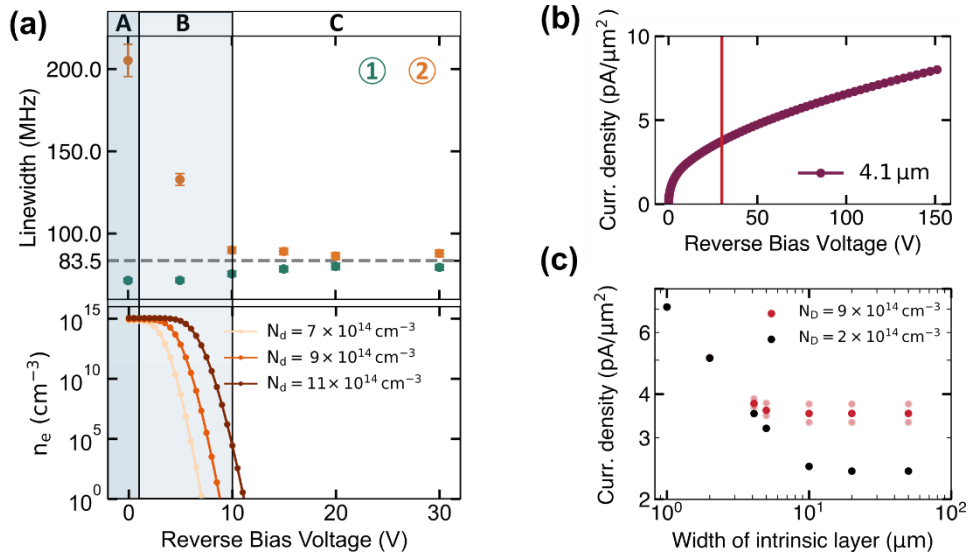


Figure 3: (a) Dependency of the linewidth on the position of the vacancy inside the intrinsic layer and the applied voltage. Upper panel: Linewidth of $V_{Si1,2}$ centers as a function of applied reverse bias voltage. Lower panel: Simulated concentration of electrons at the positions of $V_{Si1,2}$ centers. (b) Simulation of the reverse current density of the pin-diode considered here (width 4.1 μm , $N_D = 9 \times 10^{14} \text{ cm}^{-3}$) at different reverse bias voltages. (c) Simulation of the reverse current density at 30 V as a function of the width of the intrinsic layer for $9 \times 10^{14} \text{ cm}^{-3}$ (red) incorporating the uncertainty of the doping concentration (light red) and $2 \times 10^{14} \text{ cm}^{-3}$ (black).

Whereas the exact position of the PLE lines depends on the local electric field E seen by the single V_{Si} center, their optical linewidth is the result of charge fluctuations. Free charges can either stem from ionized defects, such as nearby ionized carbon vacancies²⁸, or incorporated dopants³⁶ residing in the vicinity of the V_{Si} center. The resulting electric field E_{fluc} created by the fluctuating charges couples to the permanent electric dipole moment d in the ground and excited state of the V_{Si} as $H \sim d \cdot E_{fluc}$. Therefore, the optical linewidth depends on the fluctuating electric field around the V_{Si} and a reduction of mobile charges in the local environment of the V_{Si} center causes a reduced optical linewidth of both A_1 and A_2 . This can be achieved within a *pin*-diode due to the formation of a depletion region by

applying reverse bias voltages³⁷. We find that the optical linewidth strongly depends on the position of the color centers and can range from $205.2 \pm 9.8 \text{ MHz}$ to $71.5 \pm 1.4 \text{ MHz}$ in the absence of any applied reverse bias voltage, as shown in Fig. 3(a). We attribute this behavior to the width x_n of the depletion region in the absence of an applied reverse bias voltage. As the sample's built-in voltage of $V_{bi} = 2.95 \text{ V}$ causes the depletion zone to extend $1.9 \mu\text{m}$ into the intrinsic layer, V_{Si1} ($x = 1.6 \mu\text{m}$, see Fig. 2 (a)), resides in the space-charge region of the diode, contrary to V_{Si2} ($x = 2.7 \mu\text{m}$). This indicates that – unlike V_{Si2} – the charge environment around V_{Si1} center is initially already depleted. An increase of the reverse bias voltage of the *pin*-diode shifts the depletion region further into the intrinsic area where eventually also V_{Si2} center is in the space charge region. As a consequence, the concentration of surrounding charges around V_{Si2} is significantly reduced and the optical linewidth starts to narrow. If the reverse bias voltage is increased $\geq 10 \text{ V}$, the optical linewidth of V_{Si2} center reaches its plateau of $\approx 80 \text{ MHz}$. This finding stays in good agreement with the charge depletion simulation shown in Fig. 3 (a) (bottom), indicating that free charges within the intrinsic region are fully depleted at a reverse bias voltage of $\geq 10 \text{ V}$.

Whereas the linewidth of V_{Si2} center decreases with increasing reverse bias voltage, the linewidth of V_{Si1} center gets broadened [see Fig. 3 (a) region B], which cannot be explained by the depletion of free charges within the intrinsic area. Based on FEM simulations of the *pin*-diode, it can be shown that with increasing applied reverse bias, a reverse current starts to flow [see Fig. 3 (b)]. This causes a rise of mobile charge carriers flowing in the vicinity of V_{Si1} center and therefore increases its optical linewidth. As the concentration of charges due to this current is on the order of $\sim 10^8 \text{ cm}^{-3}$ (see Supplementary Information SI9), the broadening effect is small compared to the narrowing effect of the formation of the space charge region (which reduces the charge concentration by $\sim 10^{15} \text{ cm}^{-3}$). It can be seen from Fig. 3 (a) (region C) that $V_{Si1,2}$ centers both approach a linewidth of around 80 MHz for high voltages. Here both V_{Si} are in the space charge region and the same current flows nearby. This linewidth is larger than the V_{Si} center's A_2 optical lifetime limit of 14 MHz ³⁸, which we attribute to the reverse current becoming the dominant mechanism at higher voltages. Simulations show that this effect can be minimized by using an intrinsic layer with a reduced concentration of dopants as well as an intrinsic region with a width of $\geq 10 \mu\text{m}$ [Fig. 3 (c)]. The PLE linewidth can additionally be reduced with an improved epitaxial layer quality, which reduces deep traps and thus prevents Shockley-Read-Hall generation³⁹ of charges.

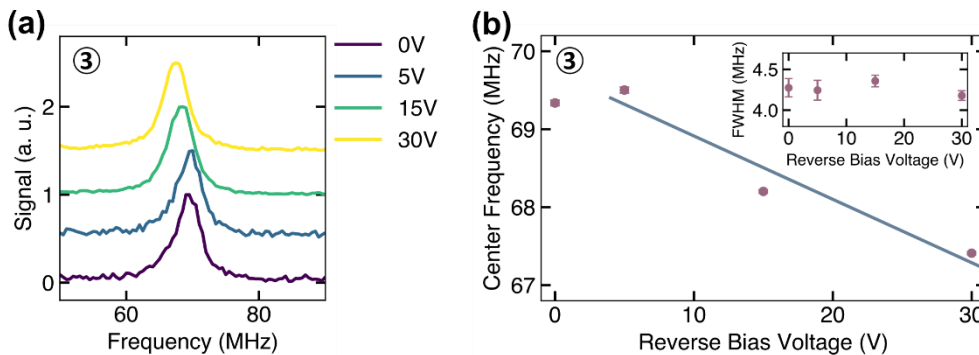


Figure 4: (a) ODMR measurement for different applied reverse bias voltages of 0 V (blue), 5 V (light-blue), 15 V (green) and 30 V (yellow). (b) The shift of the ODMR-peaks reveals that only for voltages greater than 5 V an effective field at the position of the vacancy forms, shifting the ZFS. Inset: The full width at half maximum of the ODMR-signal stays constant, which excludes broadening mechanisms at higher voltages.

To extract the influence of the reverse bias voltage onto the ground state of the V_{Si3} center, we performed ODMR measurements for reverse bias voltages from 0 V up to 30 V [see Fig. 4 (a)]. There

is a clear shift of the resonance position from the ZFS of $\approx 70 \text{ MHz}$ visible within the measurements, which is in good agreement with ODMR simulations based on Eq. (2) (see SI). The strength of the shift correlates with the applied reverse bias voltage and a gradient of $d_{GS} = -0.07 \pm 0.02 \frac{\text{Hz}}{\text{V/m}}$. The onset of the Stark shift, which has been seen in Fig. 2 (b) at around $\sim 2.6 \text{ V}$, is also present in these ODMR measurements [Fig. 4 (b)]. This method therefore allows to extract the expansion of the depletion region based on the applied reverse bias voltage at ambient temperature.

In conclusion, we have shown the local-measurement-based reconstruction of physical parameters in an electronic device, like the formation of the space charge region, the electric field, and the doping level with V_{Si} centers in 4H-SiC. The presented method allows the measurement of device characteristics with an Abbe-limited lateral spatial resolution of $\approx 500 \text{ nm}$, even far below the surface and at various positions within the semiconductor device. Silicon vacancy centers are also excellent sensors of e.g., temperature^{22,40} and magnetic fields^{21,41}, where the latter can be used to infer the current density in operating integrated circuits⁴². We envisage that V_{Si} centers enable the full operando monitoring of semiconductor devices, which can greatly help to infer the device performance characteristics and improve their performance in power electronics.

Besides applications in the electrometry of semiconductor devices, the method presented here is also of great use to establish silicon-vacancy based quantum communication networks. These protocols rely on indistinguishable photons emitted from separate quantum network nodes. This can be achieved by utilizing the presented *pin*-diodes, whose resonances are tuned such that the emitted photons have the same wavelength and two-photon interference^{43,44} can occur, which is a prerequisite for spin-spin entanglement^{45,46}.

Acknowledgement

We thank M. Bockstedte (University Linz) for helpful discussions about the Stark shift. R. Nagy acknowledges the funding of BMBF QMNDQCNet (Grant No. 13N16264), DFG (Project No. 462567933), and Lighthouse Project QuMeCo (State of Bavaria). P. Udvarhelyi and P. Narang acknowledge the support of the U.S. National Science Foundation QuSeC-TAQS under Award No. 2326840. This research used resources of the National Energy Research Scientific Computing Center, a DOE Office of Science User Facility supported by the Office of Science of the U.S. Department of Energy under Contract No. DE-AC02-05CH11231 and Award No. BES-ERCAP0029123.

Author Contributions

D. S. fabricated the *pin*-sample and carried out the IV measurements. F. H. performed the PLE and ODMR measurements. F. H. and M. H. performed the sensitivity measurement. J. S. performed the FEM simulations of the *pin*-diode and carried out the CV measurement. W. K. irradiated the sample. P. U. performed the simulations of the dipole moment and polarizability. H. W. supported sample manufacturing. M. H. performed the data analysis, the ODMR simulations, wrote the manuscript and coordinated the project. R. N. supervised the project. All authors discussed and contributed to the manuscript.

Competing interests

The authors declare no competing interests.

Data availability

The data that support the findings of this paper are available from the corresponding author upon reasonable request.

Bibliography

1. Nishikawa, A., Kumakura, K. & Makimoto, T. High Critical Electric Field Exceeding 8 MV/cm Measured Using an AlGaIn p–i–n Vertical Conducting Diode on n-SiC Substrate. *Jpn. J. Appl. Phys.* **46**, 2316 (2007).
2. De Wolf, P., Brazel, E. & Erickson, A. Electrical characterization of semiconductor materials and devices using scanning probe microscopy. *Mater. Sci. Semicond. Process.* **4**, 71–76 (2001).
3. Henning, A. K. *et al.* Two-dimensional surface dopant profiling in silicon using scanning Kelvin probe microscopy. *J. Appl. Phys.* **77**, 1888–1896 (1995).
4. Broadway, D. A. *et al.* Spatial mapping of band bending in semiconductor devices using in situ quantum sensors. *Nat. Electron.* **1**, 502–507 (2018).
5. Iwasaki, T. *et al.* Direct Nanoscale Sensing of the Internal Electric Field in Operating Semiconductor Devices Using Single Electron Spins. *ACS Nano* **11**, 1238–1245 (2017).
6. Wang, H. *et al.* A review of silicon carbide CMOS technology for harsh environments. *Mater. Sci. Semicond. Process.* **178**, 108422 (2024).
7. Cilibrizzi, P. *et al.* Ultra-narrow inhomogeneous spectral distribution of telecom-wavelength vanadium centres in isotopically-enriched silicon carbide. *Nat. Commun.* **14**, 8448 (2023).
8. Wolfowicz, G. *et al.* Vanadium spin qubits as telecom quantum emitters in silicon carbide. *Sci. Adv.* **6**, eaaz1192 (2020).
9. Rühl, M. *et al.* Removing the orientational degeneracy of the TS defect in 4H–SiC by electric fields and strain. *New J. Phys.* **23**, 073002 (2021).
10. Widmann, M. *et al.* Coherent control of single spins in silicon carbide at room temperature. *Nat. Mater.* **14**, 164–168 (2015).
11. Nagy, R. *et al.* High-fidelity spin and optical control of single silicon-vacancy centres in silicon carbide. *Nat. Commun.* **10**, 1954 (2019).
12. Christle, D. J. *et al.* Isolated Spin Qubits in SiC with a High-Fidelity Infrared Spin-to-Photon Interface. *Phys. Rev. X* **7**, 021046 (2017).

13. Nagy, R. *et al.* Narrow inhomogeneous distribution of spin-active emitters in silicon carbide. *Appl. Phys. Lett.* **118**, 144003 (2021).
14. Nagy, R. *et al.* Quantum Properties of Dichroic Silicon Vacancies in Silicon Carbide. *Phys. Rev. Appl.* **9**, 034022 (2018).
15. Morioka, N. *et al.* Spin-controlled generation of indistinguishable and distinguishable photons from silicon vacancy centres in silicon carbide. *Nat. Commun.* **11**, 2516 (2020).
16. Fang, R.-Z. *et al.* Experimental Generation of Spin-Photon Entanglement in Silicon Carbide. *Phys. Rev. Lett.* **132**, 160801 (2024).
17. Lai, X.-Y. *et al.* Single-Shot Readout of a Nuclear Spin in Silicon Carbide. *Phys. Rev. Lett.* **132**, 180803 (2024).
18. Parthasarathy, S. K. *et al.* Scalable Quantum Memory Nodes Using Nuclear Spins in Silicon Carbide. *Phys. Rev. Appl.* **19**, 034026 (2023).
19. Bourassa, A. *et al.* Entanglement and control of single nuclear spins in isotopically engineered silicon carbide. *Nat. Mater.* **19**, 1319–1325 (2020).
20. Niethammer, M. *et al.* Coherent electrical readout of defect spins in silicon carbide by photo-ionization at ambient conditions. *Nat. Commun.* **10**, 5569 (2019).
21. Kraus, H. *et al.* Magnetic field and temperature sensing with atomic-scale spin defects in silicon carbide. *Sci. Rep.* **4**, 5303 (2015).
22. Hoang, T. M. *et al.* Thermometric quantum sensor using excited state of silicon vacancy centers in 4H-SiC devices. *Appl. Phys. Lett.* **118**, 044001 (2021).
23. Anisimov, A. N. *et al.* Optical thermometry based on level anticrossing in silicon carbide. *Sci. Rep.* **6**, 33301 (2016).
24. Heiler, J. *et al.* Spectral stability of V₂ centres in sub-micron 4H-SiC membranes. *Npj Quantum Mater.* **9**, 34 (2024).
25. Babin, C. *et al.* Fabrication and nanophotonic waveguide integration of silicon carbide colour centres with preserved spin-optical coherence. *Nat. Mater.* **21**, 67–73 (2022).

26. Simin, D. *et al.* Locking of electron spin coherence above 20 ms in natural silicon carbide. *Phys. Rev. B* **95**, 161201 (2017).
27. Anderson, C. P. *et al.* Five-second coherence of a single spin with single-shot readout in silicon carbide. *Sci. Adv.* **8**, eabm5912 (2022).
28. Widmann, M. *et al.* Electrical Charge State Manipulation of Single Silicon Vacancies in a Silicon Carbide Quantum Optoelectronic Device. *Nano Lett.* **19**, 7173–7180 (2019).
29. Dolde, F. *et al.* Electric-field sensing using single diamond spins. *Nat. Phys.* **7**, 459–463 (2011).
30. Doherty, M. W. *et al.* Theory of the ground-state spin of the NV – center in diamond. *Phys. Rev. B* **85**, 205203 (2012).
31. Lukin, D. M. *et al.* Spectrally reconfigurable quantum emitters enabled by optimized fast modulation. *Npj Quantum Inf.* **6**, 80 (2020).
32. Bathen, M. E., Vines, L. & Coutinho, J. First-principles calculations of Stark shifts of electronic transitions for defects in semiconductors: the Si vacancy in 4H-SiC. *J. Phys. Condens. Matter* **33**, 075502 (2020).
33. Rühl, M., Bergmann, L., Krieger, M. & Weber, H. B. Stark Tuning of the Silicon Vacancy in Silicon Carbide. *Nano Lett.* **20**, 658–663 (2020).
34. Wrzecionko, B., Biela, J. & Kolar, J. W. SiC power semiconductors in HEVs: Influence of junction temperature on power density, chip utilization and efficiency. in *2009 35th Annual Conference of IEEE Industrial Electronics* 3834–3841 (IEEE, Porto, 2009). doi:10.1109/IECON.2009.5415122.
35. Boettcher, N. & Erlbacher, T. Design Considerations on a Monolithically Integrated, Self Controlled and Regenerative 900 V SiC Circuit Breaker. in *2020 IEEE Workshop on Wide Bandgap Power Devices and Applications in Asia (WiPDA Asia)* 1–6 (IEEE, Suita, Japan, 2020). doi:10.1109/WiPDAAsia49671.2020.9360279.
36. Son, N. T. & Ivanov, I. G. Charge state control of the silicon vacancy and divacancy in silicon carbide. *J. Appl. Phys.* **129**, 215702 (2021).
37. Anderson, C. P. *et al.* Electrical and optical control of single spins integrated in scalable semiconductor devices. *Science* **366**, 1225–1230 (2019).

38. Liu, D. *et al.* The silicon vacancy centers in SiC: determination of intrinsic spin dynamics for integrated quantum photonics. *Npj Quantum Inf.* **10**, 72 (2024).
39. Sah, C., Noyce, R. & Shockley, W. Carrier Generation and Recombination in P-N Junctions and P-N Junction Characteristics. *Proc. IRE* **45**, 1228–1243 (1957).
40. Yamazaki, Y., Masuyama, Y., Kojima, K. & Ohshima, T. Highly Sensitive Temperature Sensing Using the Silicon Vacancy in Silicon Carbide by Simultaneously Resonated Optically Detected Magnetic Resonance. *Phys. Rev. Appl.* **20**, L031001 (2023).
41. Abraham, J. B. S. *et al.* Nanotesla Magnetometry with the Silicon Vacancy in Silicon Carbide. *Phys. Rev. Appl.* **15**, 064022 (2021).
42. Garsi, M. *et al.* Three-dimensional imaging of integrated-circuit activity using quantum defects in diamond. *Phys. Rev. Appl.* **21**, 014055 (2024).
43. Bernien, H. *et al.* Two-Photon Quantum Interference from Separate Nitrogen Vacancy Centers in Diamond. *Phys. Rev. Lett.* **108**, 043604 (2012).
44. Sipahigil, A. *et al.* Quantum Interference of Single Photons from Remote Nitrogen-Vacancy Centers in Diamond. *Phys. Rev. Lett.* **108**, 143601 (2012).
45. Bernien, H. *et al.* Heralded entanglement between solid-state qubits separated by three metres. *Nature* **497**, 86–90 (2013).
46. Humphreys, P. C. *et al.* Deterministic delivery of remote entanglement on a quantum network. *Nature* **558**, 268–273 (2018).

Supplementary Information

SI1. Sample

We use a commercially available 4H-SiC wafer from JXT Technology Co., Ltd., where according to the manufacturer, on top of a highly n-type substrate, a n^{++} buffer layer (doping $1 \times 10^{18} \text{ cm}^{-3}$), an n-type epitaxial layer (doping $2 \times 10^{14} \text{ cm}^{-3}$, according to manufacturer) of $4.1 \mu\text{m}$ thickness (further referred to as “intrinsic layer” of the pin-diode) and a $2 \mu\text{m}$ thick p^{++} -epilayer with doping of $2 \times 10^{19} \text{ cm}^{-3}$ have been grown. At the n^{++} - and p^{++} -sides of the sample, Ohmic contacts were formed by Ni/Al deposition and subsequent annealing at, respectively, 1000°C for 5 minutes at the n^{++} -side and 800°C for 3 minutes at the p^{++} -side. For the n^{++} contact a layer of 50 nm Ni was used and for the p^{++} contact a composition of 53 nm Ni and 43 nm Al. To create color centers, the sample was electron irradiated with a flux of $1 \times 10^{12} \text{ cm}^{-2}$ and an energy of 4 MeV, followed by annealing at 600°C for 30 minutes.

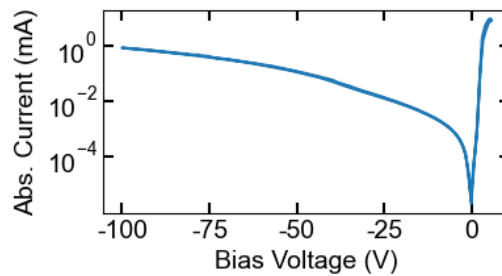


Figure (SI) 1: IV measurement of the sample, confirming the characteristics of a pin-diode with a bias voltage applied to the p^{++} -side of the sample and the n^{++} -side being grounded. The diode is operated in forward direction for positive voltages and in reverse bias for negative voltages.

To confirm the proper manufacturing of our *pin*-diode, we recorded the IV characteristics [see Fig. (SI) 1], where the n^{++} -side of the sample was grounded and a voltage was applied to the p^{++} -side. Therefore, the diode was operated in forward direction for positive voltages and in reverse bias mode for negative voltages.

CV Measurements of the Doping Concentration in the Intrinsic Layer

To measure the concentration of dopants in the intrinsic layer of our *pin*-diode, we used a sample from the same wafer as the sample that was used for the spin measurements reported in the main text. Starting from the p^{++} -side, $4.5 \mu\text{m}$ were etched away, leaving an effective epitaxial intrinsic layer of $1.6 \mu\text{m}$. On top of this layer, a Schottky contact was fabricated for the CV measurements [see Fig. (SI) 2(a)].

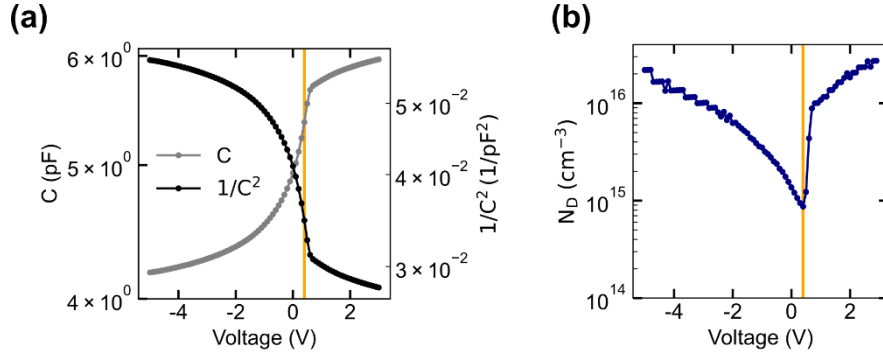


Figure (SI) 2: (a) Measurements of the capacitance C as a function of the applied voltage (V) and the corresponding $1/C^2$ values. (b) Corresponding concentration of dopants in the intrinsic layer as a function of the applied voltage. Positive voltages in (a) and (b) are in forward, negative voltages in reverse bias direction of the diode.

The CV measurements were carried out by an Agilent E4980A parameter analyzer with the voltages set around the built-in voltage of the Schottky junction. From the measured capacitance the $1/C^2$ values were determined which are inversely proportional to the doping concentration in the sample, as

$$N_D = \frac{-2}{e\epsilon_0\epsilon_r A^2} \frac{d(1/C^2)'}{dV}$$

with e the electron charge, $\epsilon_r = 9.66$ the relative permittivity of 4H-SiC, ϵ_0 the vacuum permittivity, and $A = (300 \mu\text{m})^2$ the area of the Schottky contact. In Fig. (SI) 2, two separate regions can be seen which are the reverse and forward direction of the Schottky junction. In reverse conditions, the doping of the epitaxial layer can be determined with the above equation. The doping on the surface of the etched back epitaxial layer was determined to be $8.7 \times 10^{14} \text{ cm}^{-3}$ (for 0.4 V, see orange line in Fig. (SI) 2), increasing towards the buffer layer.

SI2. Experimental Setup

For the measurements reported here, we use a home-built confocal microscope. For off-resonant excitation, a 730 nm laser (Toptica iBeam smart) is used and for resonant excitation, we use a Toptica DL Pro (916 nm). To create pulses of the resonant laser, an Acousto-Optical Modulator (AOM) from Gooch & Housego (AOMO 3200-1113) is used and the excitation light is power-stabilized at discrete time intervals through an amplitude-EOM (Jenoptik, AM905b). For excitation at both wavelengths, a dichroic mirror (Semrock FF925-Di01) reflects the excitation light and transmits the fluorescence of the color center. The excitation light is reflected at a scanning mirror (Mad City Labs, Nano-MTA2X10) and focused on the sample inside the cryostat (Attocube attodry 800) with a high-NA objective (Zeiss Epiplan-Neofluar 100x, NA 0.9). The emitted fluorescence is collected by the same objective and forwarded to the SNSPD after being highpass-filtered at 950 nm (Thorlabs FELH0950). For the orchestration of our pulse sequences, and to perform time-tagging of the detected counts from the SNSPD we use an OPX from Quantum Machines.

SI3. FEM-Simulations of Local Electric Field and Band Bending

For the simulations of the electrical properties, the commercial TCAD (vV-2023.12) software was used. The device was first built in the *sprocess* module and subsequently electrically simulated in the *sdevice* module using the Bank/Rose nonlinear solver.

The electric fields as simulated with TCAD describe the macroscopic field inside the SiC semiconductor structure. As the V_{Si} is a microscopic point defect, it is not only subject to the polarization of the medium under an applied reverse bias voltage but also to electric field contributions stemming from nearby polarized dipoles, which implies that the total electric field acting on the vacancy is¹

$$E_{tot} = E + E_i,$$

where E is the macroscopic electric field (the external electric field plus the polarization response of the lattice) and E_i is the field generated by the nearby dipoles, which follows to be^{1,2}

$$E_i = \frac{P}{3\epsilon_0}.$$

As the polarization P can be expressed in terms of the electric field E via the vacuum permittivity ϵ_0 and the relative permittivity ϵ_r as $P = \epsilon_0(\epsilon_r - 1)E$, one obtains

$$E_{tot} = E + \frac{P}{3\epsilon_0} = \frac{2 + \epsilon_r}{3}E.$$

With $\epsilon_r \approx 10$ for 4H-SiC³, one sees that $E_{tot} \approx 4E$, meaning that the actual electric field acting on the V_{Si} is four times higher than the macroscopic field obtained from the TCAD simulations.

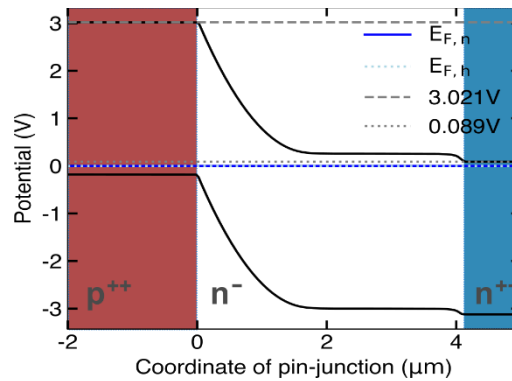


Figure (SI) 3: Simulated band structure of the *pin*-diode considered in this work. The n^- -doped layer of $4.1\mu\text{m}$ width and doping of 10^{15} cm^{-3} , in the main text denoted as ‘intrinsic layer’, is separated by a p^{++} and n^{++} region.

To obtain the built-in voltage of the *pin*-diode, we simulated the energy bands for an intrinsic doping of $1 \times 10^{15}\text{ cm}^{-3}$ [Fig. (SI) 3]. By subtracting the maximum of the conduction band from its minimum, the built-in voltage of 2.93 V can be obtained. We find that this value does not change significantly for a doping of $8 \times 10^{14}\text{ cm}^{-3}$, as considered in the main text.

SI4. Formation of Depletion zone under reverse bias voltages

The width of the depletion zone at the interface of a p- and a n-doped region into the n-doped area is

$$x_n(V) = \sqrt{\frac{2\epsilon_0\epsilon_r N_D}{e} \frac{1}{N_A N_A + N_D} (V_{bi} + V)},$$

where ϵ_0 is the vacuum permittivity, $\epsilon_r = 9.66$ the relative permittivity of 4H-SiC, e the elementary charge, V the externally applied voltage across the junction and $V_{bi} = 2.95 \text{ V}$ is the built-in voltage for the given junction. N_A (N_D) are the concentrations of acceptors (dopants). As for the device considered here the concentration of acceptors greatly exceeds the number of dopants, $N_A \gg N_D$, the above equation can be reduced to

$$x_n(V) \approx \sqrt{\frac{2\epsilon_0\epsilon_r}{e} \frac{1}{N_D} (V_{bi} + V)},$$

which shows that the length of the depletion zone depends on both the voltage being applied across the diode, as well as the doping inside the intrinsic layer.

The above equation can be used to calculate the concentration of dopants in the intrinsic layer. Rearranging for N_D leads to

$$N_D(V, x_n) = \frac{2\epsilon_0\epsilon_r}{e} \frac{V + V_{bi}}{x_n^2}.$$

V_{Si2} has a threshold voltage of $2.6 \pm 0.4 \text{ V}$ [see inset Fig. 2(b), main text] and its distance to the interface between p^{++} and intrinsic layer is $2.71 \pm 0.25 \mu\text{m}$. Note that the uncertainty of the position considers that the resolution of our confocal setup is in the order of 500 nm. With this we find the concentration to vary from $7 \times 10^{14} \text{ cm}^{-3}$ ($V = 2.2 \text{ V}, x_n = 2.71 + 0.25 \mu\text{m}$) to $11 \times 10^{14} \text{ cm}^{-3}$ ($V = 3 \text{ V}, x_n = 2.71 - 0.25 \mu\text{m}$), resulting in a doping concentration of $N_D = (9 \pm 2) \times 10^{14} \text{ cm}^{-3}$.

SI5. Additional Information about PLE-Measurements

For the underlying PLE sequence of the measurements of the Stark Shift [Fig. 2(b), main text], an initial red laser pulse at 730 nm ensures the correct charge state. Then the wavelength of the diode laser (Toptica DL Pro) is tuned through an external DC voltage. While sweeping, the wavelength of the laser is measured by a wavemeter (High Finesse WS7), and the counts are detected with an SNSPD (Single Quantum). For higher spin contrast, a microwave AC voltage at 70 MHz is applied through the copper wire in the vicinity of the color centers [see Fig. 1(b), main text]. Both resonances [see Fig. 1(d) for an example] appear as peaks in the obtained spectrum. In Fig. (SI) 4, the detuning between both resonances is plotted, where no significant deviation from $\Delta_{A_1, A_2} \approx 1 \text{ GHz}$ over the applied voltages can be found.

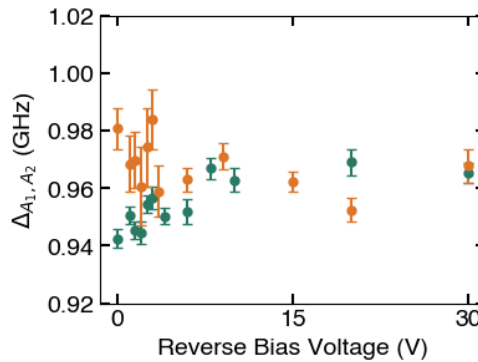


Figure (SI) 4: Detuning between the A_1 and A_2 transitions of vacancies V_{Si1} (green) and V_{Si2} (orange) for different applied voltages. The Stark shift of the A_1 transition is shown in Fig. 2(b) (main text).

The linewidths [Fig. 3(a), main text] were obtained purely optically with a phase-EOM (Exail MPX-950-LN-10), where the seed laser was detuned by +1 GHz from the A_2 transition. After a 730 nm pulse to ensure the correct charge state, the AC voltage applied to the phase-EOM was modulated from 800 MHz to 1.4 GHz, which effectively sweeps the sidebands over the A_2 transitions. The signal was fitted with a Lorentzian to obtain the FWHM as shown in Fig. 3(a).

SI6. Dipole Moments and Polarizabilities for Different Doping Concentrations

As the concentration of donors inside the intrinsic layer of the sample used for the measurements reported here has some uncertainty concerning their concentration (see CV-measurements in SI1 as well as discussion of the relation between the Stark shift threshold and the concentration in SI4), we simulated the electric field across our *pin*-diode as a function of the applied voltage for concentrations of $7 \times 10^{14} \text{ cm}^{-3}$, $9 \times 10^{14} \text{ cm}^{-3}$ and $11 \times 10^{14} \text{ cm}^{-3}$, which covers the full range of the concentration of dopants as derived in SI4.

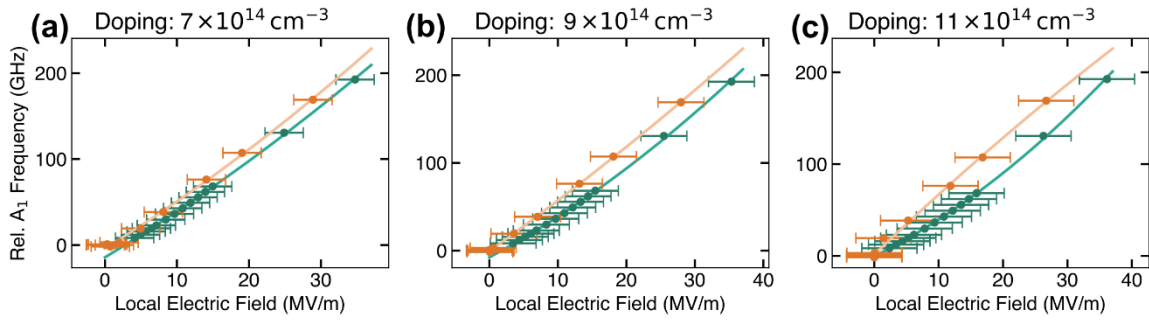


Figure (SI) 5: Stark shift of $V_{Si1,2}$ obtained from Fig. 2(b) (main text) by converting the applied voltage into the local electric field at the position of the V_{Si} center and by considering a doping of (a) $7 \times 10^{14} \text{ cm}^{-3}$, (b) $9 \times 10^{14} \text{ cm}^{-3}$ or (c) $11 \times 10^{14} \text{ cm}^{-3}$ in the simulations to cover the error of the estimated doping as given in the main text.

As one can see in Fig. (SI) 5, the Stark shift as a function of the local electric field behaves slightly differently, depending on the concentration of dopants in the intrinsic layer considered in the FEM simulations.

To extract the dipole moment d and the polarizability α , the relative A_1 frequency Δf_{A_1} is fitted by

$$\Delta f_{A_1} = -d \cdot E - \frac{\alpha}{2} E^2 + f_0. \quad (\text{SI } 1)$$

The resulting fit parameters are listed in Tab. (SI) 1. The dipole moment is slightly higher for V_{Si2} , compared to V_{Si1} , which we attribute to effects not covered by our electric field simulation, like e.g., screening effects leading to local inhomogeneities of the electric field.

(a)	$N_D = 7 \times 10^{14} \text{ cm}^{-3}$		
	$d \left(\frac{\text{GHz}}{\text{MV/m}} \right)$	$\alpha \left(\frac{\text{GHz}}{\left(\frac{\text{MV}}{\text{m}} \right)^2} \right)$	$f_0 \text{ (GHz)}$
V_{Si1}	-5.08 ± 0.14	-0.05 ± 0.01	-14.35 ± 1.00
V_{Si2}	-5.15 ± 0.41	-0.06 ± 0.03	-3.90 ± 1.38

(b)	$N_D = 9 \times 10^{14} \text{ cm}^{-3}$		
	$d \left(\frac{\text{GHz}}{\text{MV/m}} \right)$	$\alpha \left(\frac{\text{GHz}}{\left(\frac{\text{MV}}{\text{m}} \right)^2} \right)$	$f_0 \text{ (GHz)}$
V _{Si 1}	-4.21 ± 0.15	-0.09 ± 0.01	-7.73 ± 0.96
V _{Si 2}	-5.60 ± 0.13	-0.03 ± 0.01	-0.67 ± 0.42

(c)	$N_D = 11 \times 10^{14} \text{ cm}^{-3}$		
	$d \left(\frac{\text{GHz}}{\text{MV/m}} \right)$	$\alpha \left(\frac{\text{GHz}}{\left(\frac{\text{MV}}{\text{m}} \right)^2} \right)$	$f_0 \text{ (GHz)}$
V _{Si 1}	-3.46 ± 0.10	-0.11 ± 0.01	-0.49 ± 0.61
V _{Si 2}	-6.71 ± 0.39	0.03 ± 0.03	1.46 ± 1.36

Table (SI) 1: Dipole moments d and polarizabilities α extracted via the fit of Δf_{A_1} from the Stark shift measurements shown in Fig. (SI) 3 for different considered doping concentrations in the intrinsic layer.

S17. First-principles calculations of dipole moment and polarizability

We apply first-principles calculations to accurately characterize the changes in the dipole moment and polarizability during the excitation process in the k -V_{Si} defect. As opposed to the method in Ref. ⁴, we use the modern theory of polarization⁵ to extract these properties from bulk calculations instead of the simulation of a hydrogen-terminated thin surface model. Furthermore, we obtain these values directly from the calculated macroscopic dipole moment and its variation, as well as from the calculated ZPL shift in the presence of a local electric field in the crystal. The former method is expected to estimate the properties of the V₂ center more accurately, as the calculated ZPL energy suffers from the bandgap problem common in local functional calculations. We apply density functional theory (DFT) calculations using the PBE functional⁶ as implemented in Quantum Espresso⁷⁻⁹. Plane-wave and charge density cutoffs of 80 and 320 Ry were used, respectively. Core electrons were treated using Optimized Norm-Conserving Vanderbilt (ONCV) pseudopotentials^{10,11}. The defect is modeled in a large 576-atom supercell model of bulk 4H-SiC. Owing to the Brillouin zone folding, we sample only the Gamma point of the reciprocal space. The ground and first excited state of the V₂ center is calculated in the Δ SCF method¹² with the relaxation of the atomic positions. A local electric field is applied along the symmetry axis of the defect (c -axis) reflecting the experimental setup. Thus, we calculate the change in the axial component (z) of the dipole moment vector ($\Delta d_z = d$) and the polarizability matrix ($\Delta \alpha_{zz} = \alpha$) in the excitation process. The piezo effect is not calculated, i.e., the optimized ground and excited state geometries are not relaxed further in the presence of the electric field. Our results [see Fig. (SI) 6] show a linear electric field dependence of d , suggesting that the second-order expansion of the Stark shift in Eq. (3) accurately describes the measured ZPL energy shift. From the linear fit to our calculation data and its standard error, we determine $d = 1.83 \pm 0.01 \frac{\text{GHz}}{\left(\frac{\text{MV}}{\text{m}} \right)}$ and $\alpha = -0.0254 \pm 0.0006 \frac{\text{GHz}}{\left(\frac{\text{MV}}{\text{m}} \right)^2}$. The differences from our measured values are probably related to the functional used in the calculation and to piezo effects. As these improvements in the calculation method are orders of magnitude more expensive, they are beyond the scope of our current study.

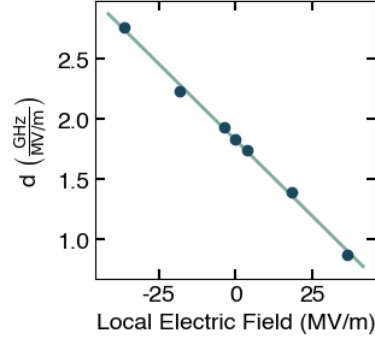


Figure (SI) 6: Simulation of the electric field dependence on the dipole moment.

S18. Sensitivity of Stark Shift Measurements

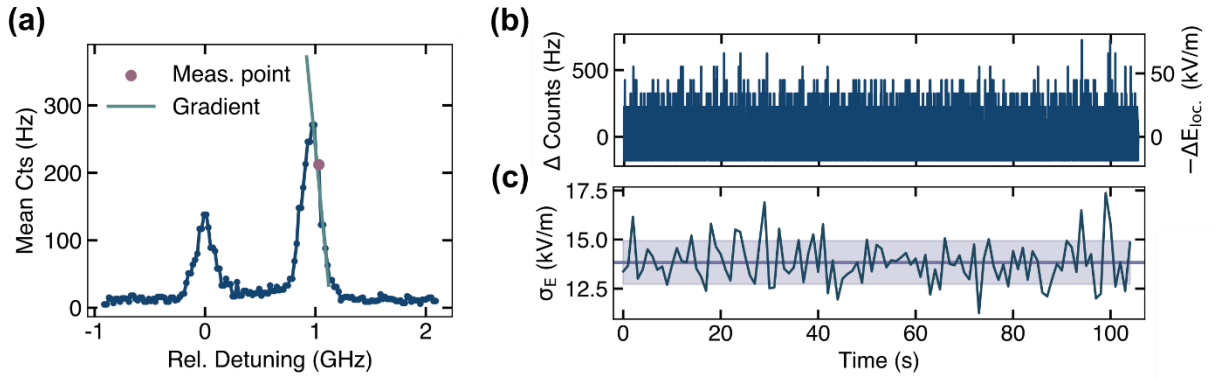


Figure (SI) 7: (a) To infer the sensitivity of the Stark shift measurements of Fig. 2(b,c) (main text), a PLE measurement at V_{Si2} was performed with 30 V applied to the diode in reverse bias. The red point represents the maximum gradient, having the highest sensitivity. (b) Counts converted into electric field fluctuations. (c) Standard deviation of (b) in 1s intervals.

To infer the sensitivity of the Stark shift measurements shown in Fig. 2(b,c), we performed a PLE measurement [Fig. (SI) 7(a)] at 30 V applied to V_{Si2} (see main text). At the maximum of its gradient (red dot in Fig. (SI) 7(a)), a time series was recorded for more than 100 seconds [Fig. (SI) 7(b)] with a sampling rate of 100 Hz.

To convert the measured photoluminescence fluctuations at that point $\Delta cts(t)$ [Fig. (SI) 7 (b)] into electric field fluctuations $\Delta E(t)$, one can use that

$$\Delta E(t) = \frac{dE}{df} \cdot \left. \frac{df}{dcts} \right|_{WP} \Delta cts(t).$$

The gradient at the working point (WP , see Fig. (SI) 7 (a)), $grad = dcts/df$, can be converted into $dcts/df|_{WP} = 1/grad$ due to the linearity of the PLE around this point. To infer the gradient of the electric field with respect to the frequency, we use that for 30 V one has $d \cdot E \gg \frac{\alpha}{2} E^2, f_0$, such that from Eq. (SI 1) it follows that

$$\frac{dE}{df} = \frac{1}{df/dE} = \frac{1}{-d'}$$

which allows to convert the fluctuations of counts into electric field fluctuations [Fig. (SI) 7(b)]. The sensitivity is then given as the mean value of the standard deviations of these electric field fluctuations within 1s intervals [Fig. (SI) 7(c)], which we find to be

$$\eta = 13.84 \pm 1.10 \frac{\text{kV/m}}{\sqrt{\text{Hz}}}.$$

This value is higher than the sensitivity reported by Ref. ¹³ for Stark-shift measurements of divacancies, but comparable to electric field sensing experiments with single NV-centers in bulk diamond¹⁴.

S19. Estimation of Linewidth-Broadening due to Reverse Current

The current as displayed in Fig. 3(b) (main text) was simulated from the number of charge carriers having flown through a cross section of 1 cm^2 . Their concentration within measurement time τ can thus be inferred as

$$n_e = \frac{j}{q \cdot v_e},$$

where j is the current density and q the electron charge and v_e the drift velocity of electrons in 4H-SiC, which was simulated to be $v_e \sim 10^7 \frac{\text{cm}}{\text{s}}$ for elevated applied reverse voltages. Using the current density as displayed in Fig. 3(b) (main text), one obtains an electron density on the order of $\sim 10^8 \text{ cm}^{-3}$, as depicted in Fig. (SI) 8.

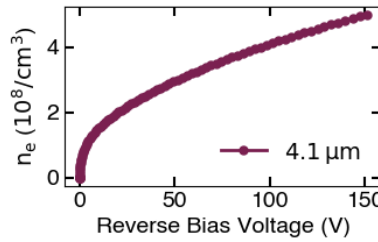


Figure (SI) 8: Electron density due to the reverse current flowing through the pin-diode.

SI10. ODMR Simulations

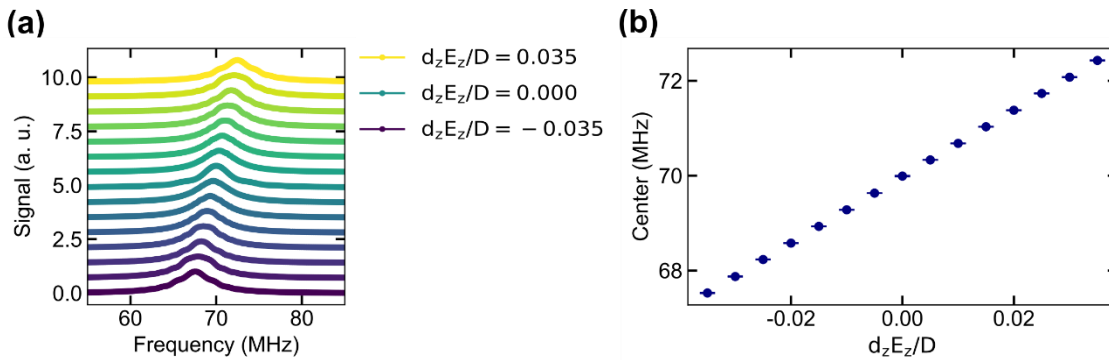


Figure (SI) 9: (a) Simulated ODMR for $d_z E_z / D$ ranging from -0.035 to 0.035 in steps of 5×10^{-3} . (b) Extracted center positions of the ODMR peaks from (a), showing linear dependence on the axial electric field E_z .

For a deeper understanding of the ODMR results presented in Fig. 4 (main text), we perform simulations with the open-source Python package QUTiP^{15,16} and consider the ground state of the V_2 center to be described by^{14,17}

$$H_{gs} = (D + d_z E_z) S_z^2.$$

Here $2D = 70 \text{ MHz}$ is the V_2 -center's ZFS, $d_z E_z$ is the electric field component along the c-axis of the lattice. Effects of transverse electric fields $E_{x,y}$ are neglected due to the device geometry.

After ensuring the correct charge state with a 730 nm laser pulse, we measured resonant ODMR where the frequency of the applied microwave field is varied while the system is read out with a laser pulse resonant with A_2 . As we start with a microwave frequency which does not cause any transition between $|\pm 1/2\rangle$ and $|\pm 3/2\rangle$, the A_2 laser effectively pumps the V_2 center into $|\pm 1/2\rangle$, which causes the initial state to be $\rho_{init} = \frac{1}{2} \left[\left| +\frac{1}{2} \right\rangle \left\langle +\frac{1}{2} \right| + \left| -\frac{1}{2} \right\rangle \left\langle -\frac{1}{2} \right| \right]$. Only if the microwave drives a transition from $|\pm 1/2\rangle$ to $|\pm 3/2\rangle$ a photon is detected, which is why we calculate the expectation value of the time-evolved state with $\frac{1}{2} \left[\left| +\frac{3}{2} \right\rangle \left\langle +\frac{3}{2} \right| + \left| -\frac{3}{2} \right\rangle \left\langle -\frac{3}{2} \right| \right]$. As can be seen from Fig. (SI) 9, the central ODMR peak is shifted towards higher values for positive and reduced from 70 MHz for negative electric fields.

Bibliography

1. Jackson, J. D. *Klassische Elektrodynamik*: (DE GRUYTER, 2006). doi:10.1515/9783110200034.
2. Stoneham, A. M. *Theory of Defects in Solids*. (Oxford University Press, 2001).
doi:10.1093/acprof:oso/9780198507802.001.0001.
3. Cheng, L., Yang, J.-Y. & Zheng, W. Bandgap, Mobility, Dielectric Constant, and Baliga's Figure of Merit of 4H-SiC, GaN, and β -Ga₂O₃ from 300 to 620 K. *ACS Appl. Electron. Mater.* **4**, 4140–4145 (2022).
4. Bathen, M. E., Vines, L. & Coutinho, J. First-principles calculations of Stark shifts of electronic transitions for defects in semiconductors: the Si vacancy in 4H-SiC. *J. Phys. Condens. Matter* **33**, 075502 (2020).
5. King-Smith, R. D. & Vanderbilt, D. Theory of polarization of crystalline solids. *Phys. Rev. B* **47**, 1651–1654 (1993).
6. Perdew, J. P., Burke, K. & Ernzerhof, M. Generalized Gradient Approximation Made Simple. *Phys. Rev. Lett.* **77**, 3865–3868 (1996).
7. Giannozzi, P. *et al.* QUANTUM ESPRESSO: a modular and open-source software project for quantum simulations of materials. *J. Phys. Condens. Matter* **21**, 395502 (2009).
8. Giannozzi, P. *et al.* Advanced capabilities for materials modelling with Quantum ESPRESSO. *J. Phys. Condens. Matter* **29**, 465901 (2017).
9. Giannozzi, P. *et al.* Quantum ESPRESSO toward the exascale. *J. Chem. Phys.* **152**, 154105 (2020).
10. Hamann, D. R. Optimized norm-conserving Vanderbilt pseudopotentials. *Phys. Rev. B* **88**, (2013).
11. Schlipf, M. & Gygi, F. Optimization algorithm for the generation of ONCV pseudopotentials. *Comput. Phys. Commun.* **196**, 36–44 (2015).
12. Gali, A., Janzén, E., Deák, P., Kresse, G. & Kaxiras, E. Theory of Spin-Conserving Excitation of the N–V–Center in Diamond. *Phys. Rev. Lett.* **103**, (2009).
13. Anderson, C. P. *et al.* Electrical and optical control of single spins integrated in scalable semiconductor devices. *Science* **366**, 1225–1230 (2019).

14. Dolde, F. *et al.* Electric-field sensing using single diamond spins. *Nat. Phys.* **7**, 459–463 (2011).
15. Johansson, J. R., Nation, P. D. & Nori, F. QuTiP: An open-source Python framework for the dynamics of open quantum systems. *Comput. Phys. Commun.* **183**, 1760–1772 (2012).
16. Johansson, J. R., Nation, P. D. & Nori, F. QuTiP 2: A Python framework for the dynamics of open quantum systems. *Comput. Phys. Commun.* **184**, 1234–1240 (2013).
17. Doherty, M. W. *et al.* Theory of the ground-state spin of the NV – center in diamond. *Phys. Rev. B* **85**, 205203 (2012).